





Asymmetric electron angular distributions in H₂ induced by intense ultrashort soft-x-ray laser pulses

Arturo Sopena ^{1,2} Fabrice Catoire ^{2,*} Alicia Palacios ^{1,3} Fernando Martín, ^{1,4,5,†} and Henri Bachau ^{2,‡}

¹*Departamento de Química, Módulo 13, Universidad Autónoma de Madrid, 28049 Madrid, Spain*

²*Centre des Lasers Intenses et Applications, Université de Bordeaux, CNRS, CEA, 33405 Talence Cedex, France*

³*Institute for Advanced Research in Chemical Sciences, Universidad Autónoma de Madrid, 28049 Madrid, Spain*

⁴*Instituto Madrileño de Estudios Avanzados en Nanociencia, Cantoblanco, 28049 Madrid, Spain*

⁵*Condensed Matter Physics Center, Universidad Autónoma de Madrid, 28049 Madrid, Spain*



(Received 3 November 2021; accepted 24 January 2022; published 11 March 2022)

X-ray free-electron-laser facilities generate nowadays ultrashort pulses with intensities as high as 10^{20} W/cm². The interaction of these light sources with atoms and molecules thus opens the way to still unexplored phenomena, where the commonly employed dipole approximation breaks down, and nonlinear excitation and ionization, e.g., Raman and Compton-like processes, come into play. We have developed theoretical tools to describe the interaction of intense attosecond soft-x-ray pulses with the hydrogen molecule in the photon energy ranging from 0.5 to 1.6 keV. We solve the time-dependent Schrödinger equation including both dipole and nondipole terms to obtain single-ionization photoelectron spectra differential in both energy and angle of the ejected electron. The signature of stimulated Compton scattering is clearly seen in the photoelectron spectra just above the ionization threshold, where nondipole effects manifest. Remarkably, the interference between dipole- and nondipole-induced quantum paths leads to a significant asymmetry of the photoelectron angular distributions. We show that this asymmetry strongly depends on the relative direction of the light polarization and propagation vectors with respect to the molecular orientation.

DOI: [10.1103/PhysRevA.105.033104](https://doi.org/10.1103/PhysRevA.105.033104)

I. INTRODUCTION

The past two decades have seen the advent of x-ray free-electron lasers (XFELs) throughout the world [1–8]. These facilities provide ultrashort pulses with unprecedented intensities (10^{20} W/cm²), over a large range of photon energies going from VUV to hard x rays. X-ray free-electron lasers can now routinely produce ultrabright few-femtosecond pulses, allowing for an increasing number of applications in atomic and molecular physics, chemistry, materials science, and biology [9–11]. Besides the impressive achievements in terms of brilliance, recent efforts are focusing on the generation and control of XFEL pulses with subfemtosecond (i.e., attosecond) durations [12]. For instance, single-spike XFEL pulses with pulse durations as short as 200 as have already been produced for photon energies in the range 4–10 keV [13]. We note that the field of attoscience has been mainly driven by high-order harmonic generation (HHG) sources [14], which nowadays can produce pulses with durations as short as 43 as and have recently reached the soft-x-ray spectral range [15–17]. However, production of x-ray pulses from HHG is still very challenging due to the low conversion efficiency of the HHG process in this energy range.

Extending the capabilities of XFELs to the attosecond domain is of crucial importance to perform real-time observations of electronic rearrangements in atoms after core excitation or ionization [13,18,19]. Two-color time-resolved x-ray spectroscopy has been proposed to explore charge migration phenomena [20] or, as demonstrated in recent experiments, to retrieve images of the Auger-Meitner decay [21] in molecules with subfemtosecond resolution. In addition, the high intensities of ultrashort XFEL pulses offer new perspectives [22–25] to study a manifold of nonlinear processes, e.g., direct two-photon ionization in Ne⁸⁺ [26] or nonlinear Compton scattering in solid Be [27].

Soft-x-ray pulses generated in synchrotrons have been recently employed in combination with multicoincident detection techniques, namely cold-target recoil-ion momentum spectrometer [28], to retrieve for the first time fully differential Compton scattering (CS) cross sections in helium [29] and to measure photoemission time delays in H₂ with zeptosecond resolution [30]. The use of ultrashort XFEL pulses can bring new scenarios for Compton scattering due to their large bandwidth, as shown by recent theoretical work on stimulated Raman scattering from atoms [31,32]. In this process, an x-ray photon is absorbed and another less energetic x-ray photon is emitted through a stimulated process in which the energy difference between the two photons is taken by a bound electron, which ends at an excited state. Stimulated emission is possible whenever photons with the energy of the emitted one are contained in the incoming light. When the energy difference between the two photons exceeds the ionization potential

*fabrice.catoire@u-bordeaux.fr

†fernando.martin@uam.es

‡hbachau@orange.fr

of the system, the process is similar to CS except that the second step is not a spontaneous process but a stimulated one and therefore is expected to lead to a strong contribution as compared to the unstimulated counterpart. Hence this process is called stimulated Compton scattering (SCS) [33]. Owing to the close connection between the two processes, the CS cross sections can be easily obtained from the SCS ionization rate [see Eq. (15) in [34]]. Stimulated CS can be a very efficient process when ultrashort pulses are used because their large bandwidth provides a wide range of photon energies to allow for x-ray stimulated emission and the ejection of low-energy electrons, for which the CS cross section is maximum [35]. Furthermore, the high intensity and repetition rate of XFELs make them an ideal tool for multicoincidence detection, which is essential to determine the molecular orientation with respect to the light polarization direction in a photoionization event [30].

In this article we present a scheme of SCS from the H_2 molecule using an intense ultrashort x-ray pulse. This work follows a recent work [36] where SCS from H_2 was investigated in the few-hundred-eV (~ 0.5 keV) energy range. In the present work we extend the previous study with a thorough investigation of this process for photon energies ranging from 0.5 to 1.6 keV, with a focus on the dipole and nondipole contributions in photoelectron energy and angular distributions. We also describe in detail the theoretical methods that are required to include such a nonlinear process, with emphasis on the necessary extensions in comparison with the usual dipole approximation. The short wavelength of the x-ray pulse breaks down the commonly employed dipole approximation and, as a consequence, the coherent contributions of dipole and nondipole terms lead to pronounced asymmetries in the photoelectron emission, which strongly depend on the x-ray wavelength and on the molecular orientation. This is a pure nonlinear effect that is better captured in the low-energy region of the photoelectron spectrum. The methodological and numerical details are given in Sec. II. In Sec. III we present our results for the energy and angle differential ionization probabilities for different orientations of the light polarization and propagation vectors with respect to the molecular axis. Our results show strong variations of these distributions with the relative orientation of the light vector with respect to the molecular axis, as well as the effect of having two emitting centers. The main conclusions are summarized in Sec. IV.

II. METHODOLOGY

The methodology used to describe the electronic structure of the isolated molecule and to solve the time-dependent Schrödinger equation (TDSE) has been described in detail in previous publications [37–40]. In the present work the method is extended to incorporate the explicit evaluation of nondipole corrections. In brief, the time-dependent wave function that represents the dynamics induced in the hydrogen molecule by an intense x-ray pulse (see Sec. II A) is expanded in the basis of two-electron states built from antisymmetrized products of one-electron molecular orbitals, as explained in Secs. II B and II C. This representation allows us to greatly reduce the computational effort and has proven to provide a very accurate representation of manifold previously investigated

light-induced processes in H_2 [39]. In this study we mainly focus on disentangling the light parameters and molecular orientation dependences of the relative contributions of dipole terms and the newly incorporated nondipole terms in the energy and angle-resolved electron emission. Due to the short duration of the x-ray pulses considered in our study, we will work within the fixed nuclei approximation. Atomic units (a.u.) are used throughout this paper unless otherwise stated.

A. Description of the laser- H_2 interaction

The nonrelativistic Hamiltonian representing the interaction of the H_2 molecule with a classical electromagnetic field is written, in the Coulomb gauge, as

$$\mathcal{H}(t) = \mathcal{H}_{el}(\mathbf{r}_1, \mathbf{r}_2) + \sum_{i=1,2} \mathbf{A}(\mathbf{r}_i, t) \cdot \mathbf{P}_i + \frac{1}{2} \sum_{i=1,2} \mathbf{A}(\mathbf{r}_i, t)^2, \quad (1)$$

where \mathcal{H}_{el} is the two-electron Hamiltonian of the isolated molecule, \mathbf{P}_i is the momentum operator for the electron i , and $\mathbf{A}(\mathbf{r}_i, t) = A(t - \boldsymbol{\eta} \cdot \mathbf{r}_i/c) \boldsymbol{\epsilon}$ is the vector potential, where $\boldsymbol{\epsilon}$ and $\boldsymbol{\eta}$ are the unitary vectors associated with the polarization, which is linear in this work, and the propagation direction of the field, respectively. Further, \mathcal{H}_{el} is given by

$$\mathcal{H}_{el}(\mathbf{r}_1, \mathbf{r}_2) = -\frac{1}{2} \sum_{i=1,2} \nabla_i^2 - \sum_{i=1,2} \left[\frac{1}{|\frac{\mathbf{R}}{2} - \mathbf{r}_i|} + \frac{1}{|\frac{\mathbf{R}}{2} + \mathbf{r}_i|} \right] + \frac{1}{|\mathbf{r}_1 - \mathbf{r}_2|} + \frac{1}{R}, \quad (2)$$

where the vectors \mathbf{r}_1 and \mathbf{r}_2 refer to the positions of electrons 1 and 2, respectively, in the center of mass, \mathbf{R} is the internuclear separation vector, and R is the internuclear distance.

We approximate $A(t - \boldsymbol{\eta} \cdot \mathbf{r}_i/c)$ in Eq. (1) by the two lowest-order terms of the Taylor expansion in $\boldsymbol{\eta} \cdot \mathbf{r}_i/c$,

$$A(t - \boldsymbol{\eta} \cdot \mathbf{r}_i/c) \simeq A(t) + F(t) \boldsymbol{\eta} \cdot \mathbf{r}_i/c, \quad (3)$$

with $F(t) = -\dot{A}(t)$. Hence, by neglecting the $1/c^2$ contributions, the Hamiltonian (1) can be rewritten

$$\mathcal{H} = \mathcal{H}_{el}(\mathbf{r}_1, \mathbf{r}_2) + A(t) \sum_{i=1,2} \boldsymbol{\epsilon} \cdot \mathbf{P}_i + A(t)F(t) \sum_{i=1,2} \boldsymbol{\eta} \cdot \mathbf{r}_i/c + A(t)^2/2. \quad (4)$$

The last term $A(t)^2/2$ can be removed by performing a gauge transformation and therefore will not be explicitly considered in the following. In Eq. (4) the term $\sum_{i=1,2} \mathbf{A}(\mathbf{r}_i, t) \cdot \mathbf{P}_i$ [see Eq. (1)] is treated in dipole approximation for reasons explained in Sec. II D. The vector potential amplitude $A(t)$ is written as

$$A(t) = f(t)A_0 \cos(\omega_0 t), \quad (5)$$

where ω_0 is the central laser frequency, A_0 is the peak amplitude of the vector potential, corresponding to a peak electric field $E_0 = A_0\omega_0$, i.e., an intensity $I = c|E_0|^2/8\pi$ (with $E_0 = 1$ a.u., corresponding to an intensity of 3.51×10^{16} W/cm²), and $f(t)$ is the pulse envelope, which has been chosen to be Gaussian. In this work we set the intensity equal to 10^{18} W/cm².

We use the approximate Hamiltonian (4) to solve the TDSE that describes the laser- H_2 interaction

$$i \frac{\partial}{\partial t} \Psi(t) = \mathcal{H}(t) \Psi(t) \quad (6)$$

by expanding the time-dependent wave function $\Psi(t)$ in the basis of H_2 eigenstates Ψ_n^Λ with eigenenergies E_n^Λ (see Sec. II B) so that

$$\Psi(t) = \sum_{n,\Lambda} C_{n,\Lambda}(t) \Psi_n^\Lambda(\mathbf{r}_1, \mathbf{r}_2) \exp(-iE_n^\Lambda t). \quad (7)$$

After injection of the above expansion into Eq. (6) and projection onto the $\Psi_n^\Lambda(\mathbf{r}_1, \mathbf{r}_2)$ states, we obtain a system of coupled differential equations that is integrated from $t = -T$ to $t = T$ using an explicit time-adaptive Runge-Kutta method, with the initial condition (at $t = -T$) corresponding to H_2 in the ground state ($X^1\Sigma_g^+$). Here T is chosen large enough such that the vector potential amplitudes $A(-T)$ and $A(T)$ vanish. The wave function $\Psi(T)$ contains all the information on the molecular system at the end of the interaction. Relevant observables like photoelectron spectra or electron angular distributions are extracted by projecting $\Psi(T)$ onto field-free states, i.e., from the expansion coefficients $C_{n,\Lambda}(T)$ associated with the eigenstates $\Psi_n^\Lambda(\mathbf{r}_1, \mathbf{r}_2)$ [39].

The procedure described above, performed in the velocity gauge with a multipole expansion of the vector potential, has been shown to be very efficient from the numerical point of view. Note that, as in the case of the dipole approximation, a transformation can be performed between the velocity and length gauges preserving the gauge invariance for an arbitrary n th-order expansion of the vector potential [41]. A review of gauge invariance theory beyond the dipole approximation is also provided in [42].

B. Two-electron states of the H_2 molecule

We only consider states of singlet spin multiplicity ($S = 0$), since these are the only ones that can be populated in the nonrelativistic limit. We use a configuration-interaction (CI) procedure to calculate the bound states of H_2 at the equilibrium internuclear distance. Each term in the CI expansion is built as a symmetrized product of H_2^+ one-electron wave functions ψ_n^m ,

$$\begin{aligned} \psi_{n_1, n_2}^{\Lambda, m_1, m_2}(\mathbf{r}_1, \mathbf{r}_2) \\ = \frac{1}{\sqrt{2}} \{ \psi_{n_1}^{m_1}(\mathbf{r}_1) \psi_{n_2}^{m_2}(\mathbf{r}_2) + \psi_{n_1}^{m_1}(\mathbf{r}_2) \psi_{n_2}^{m_2}(\mathbf{r}_1) \}, \end{aligned} \quad (8)$$

where we have factored out the spin component, which is antisymmetric, thus ensuring the antisymmetry of the two-electron configuration. The spatial component of the two-electron states are thus given by

$$\Psi_n^\Lambda(\mathbf{r}_1, \mathbf{r}_2) = \sum_{\substack{m_1, m_2 \\ \Lambda = |m_1 + m_2|}} \sum_{n_1, n_2} C_{n, n_1, n_2}^{m_1, m_2} \psi_{n_1, n_2}^{\Lambda, m_1, m_2}(\mathbf{r}_1, \mathbf{r}_2). \quad (9)$$

The coefficients $c_{n, n_1, n_2}^{m_1, m_2}$ and the eigenenergies E_n^Λ are obtained from a standard diagonalization procedure.

Note that the two-electron states are characterized by the quantum number Λ , which represents the absolute value of the z component of the total angular momentum $L_z = l_{1,z} + l_{2,z}$,

$\Lambda = 0$ (Σ), $\Lambda = 1$ (Π), $\Lambda = 2$ (Δ), etc., and the inversion symmetry of the states: gerade (g) or ungerade (u). We also note that there exists an additional symmetry associated with the reflection invariance of the Hamiltonian with respect to any plane containing the internuclear axis. According to this property, the Σ states are labeled $\Sigma_{g,u}^+$, for which the wave function is left unchanged upon reflection, or $\Sigma_{g,u}^-$ if it changes sign in performing that operation. The ground state of H_2 is denoted by $X^1\Sigma_g^+$. As explained in the following sections, the selection rules imposed by the operators describing the light-matter interaction require the evaluation of bound and continuum states of $^1\Sigma_{g,u}^+$, $^1\Pi_u$, and $^1\Delta_g$ molecular symmetries.

The evaluation of the two-electron single-continuum states requires special treatment, since a direct diagonalization on a two-electron basis does not lead to the correct asymptotic behavior. The procedure has been explained in [38], so here we only recall the main steps. First, we determine two-electron uncoupled-continuum states $\psi_E^{v\lambda lm}$ (UCSs) associated with each partial wave l in each open ionization channel v with symmetry λ (the z component of the angular momentum l_z and the inversion symmetry of the remaining electron). The scattering states with proper incoming boundary conditions are related to the UCSs through the well-known Lippmann-Schwinger equation

$$\psi_{v\lambda lm, E}^- = \psi_E^{v\lambda lm} + G^-(E) V \psi_E^{v\lambda lm}, \quad (10)$$

where $G^-(E)$ is the usual Green's function $G^-(E) = (E + i\gamma - \mathcal{H}_{el})^{-1}$, with $\gamma \rightarrow 0^-$, and V is the interchannel coupling. Using the closure relation and the basis of UCSs, Eq. (10) leads to a system of linear equations that is then solved for each energy E in the continuum.

For the calculation of the bound states, we include between 390 and 700 configurations built from H_2^+ orbitals, depending on the symmetry of the two-electron wave function. To improve the description of the ground state at the equilibrium distance $R_e \sim 1.4$ a.u., a supplementary basis set of Slater-type orbitals is included in the CI expansion. These additional basis functions are of the form $r^n e^{-\gamma_{nl} r} Y_l^m(\theta, \phi)$, with $n = 1-10$, $l = 0-11$, and $\gamma_{nl} = 2.8$ for all n and l . Each UCS of H_2 is built from 280 configurations representing an electron in a given state of H_2^+ and a scattered electron with angular momentum l . This configuration basis allows us to properly describe continuum wave functions up to an electron energy of 80 a.u. Given the high electronic energies considered in this work, the multichannel character of the wave function has to be thoroughly examined, especially with regard to the number of ionization thresholds included. We found that, if one is interested in measurements of photoelectron spectra and photoelectron angular distributions that do not distinguish between dissociative and nondissociative channels, only the first ionization threshold $1s\sigma_g$ and partial waves up to $l = 7$ need to be considered.

C. One-electron states of H_2^+

The one-electron molecular orbitals of H_2^+ used to build the two-electron configurations are the solution of the

Schrödinger equation

$$h_{el}\psi_n = E_n\psi_n, \quad (11)$$

where h_{el} is the nonrelativistic one-electron Hamiltonian of H_2^+ given by

$$h_{el}(\mathbf{r}) = -\frac{1}{2}\nabla^2 - \frac{1}{|\frac{\mathbf{R}}{2} - \mathbf{r}|} - \frac{1}{|\frac{\mathbf{R}}{2} + \mathbf{r}|} + \frac{1}{R}. \quad (12)$$

The vector \mathbf{r} refers to the electron position in the center of mass.

This equation is solved by expanding the electronic wave function ψ_n in a basis of radial B splines multiplied by spherical harmonics. If the direction of the internuclear axis is taken along the z axis, then ψ_n is also an eigenfunction of the operator l_z with eigenvalues $m = 0, \pm 1, \pm 2, \dots$. The expansion reads

$$\psi_n^m(\mathbf{r}) = \sum_{l=0}^{l_{\max}} \sum_{i=1}^{N_l} c_{il}^n \frac{B_i^k(r)}{r} Y_l^m(\theta, \phi), \quad (13)$$

where N_l is the number of B -spline functions $B_i^k(r)$. The B splines are piecewise polynomials of order k defined in a box of length r_{\max} [37]. Substitution of the expansion (13) into Eq. (11) and projection onto the $B_i^k(r)Y_l^m(\theta, \phi)$ basis leads to a generalized eigensystem problem. A diagonalization procedure is used to calculate the coefficients c_{il}^n in Eq. (13), providing a set of eigenfunctions ψ_n^m and associated eigenenergies E_n^m . In the expansion (13), the inversion symmetry affects only the spherical harmonic $Y_l^m(\theta, \phi)$, so only even (odd) values of the angular momentum contribute to orbitals of gerade (ungerade) symmetry.

For the one-center spherical expansion of the H_2^+ orbitals, we use a set of 280 B splines of order 8 and spherical harmonics up to $l = 16$. The B -spline functions are defined in an electronic radial box of length $|\mathbf{r}_{\max}| = 60$ a.u. with $\psi_n^m(\mathbf{r}_{\max}) = 0$ and the proper boundary conditions at the origin.

D. Transitions induced by the laser interaction

In order to rationalize the different coupling terms in Eq. (1), we recall the expression for stimulated Compton transition amplitudes in second order of perturbation theory. We consider a transition between a bound state $|g\rangle$ and a final state $|f\rangle$ of energies E_g and E_f , respectively. We choose a field polarization along the z axis of the reference system ($\mathbf{e} \cdot \mathbf{P}_i = P_{i,z}$); the generalization to other polarization directions is straightforward. The transition amplitude has the general form [32]

$$\mathcal{A}_{gf} \propto \int_{\omega_{fg}/2}^{\infty} d\omega \tilde{A}(\omega) \tilde{A}(\omega_{fg} - \omega) \mathcal{M}_{fg}^{\text{KHW}}(\omega, \omega - \omega_{fg}), \quad (14)$$

where $\tilde{A}(\omega)$ is the Fourier transform of the vector potential amplitude $A(t)$ and $\omega_{fg} = E_f - E_g$. In addition, $\mathcal{M}_{fg}^{\text{KHW}}(\omega, \omega - \omega_{fg})$ refers to the Kramers-Heisenberg-Waller matrix element [43,44] which defines the differential cross section for Compton scattering from a bound state [45]. It

reads

$$\begin{aligned} \mathcal{M}_{fg}^{\text{KHW}}(\omega, \omega') &= \langle f | \sum_j e^{-i\mathbf{k}' \cdot \mathbf{r}_j} P_{j,z} G^{(+)}(E_g + \omega) \sum_j e^{i\mathbf{k} \cdot \mathbf{r}_j} P_{j,z} | g \rangle \\ &+ \langle f | \sum_j e^{i\mathbf{k} \cdot \mathbf{r}_j} P_{j,z} G^{(+)}(E_g - \omega') \sum_j e^{-i\mathbf{k}' \cdot \mathbf{r}_j} P_{j,z} | g \rangle \\ &+ \sum_j \langle f | e^{i(\mathbf{k} - \mathbf{k}') \cdot \mathbf{r}_j} | g \rangle. \end{aligned} \quad (15)$$

Here $G^+(E) = (E + i\gamma - \mathcal{H}_{el})^{-1}$, with $\gamma \rightarrow 0^+$, is the so-called Green's function. The two frequencies ω and ω' are connected by $\omega - \omega' = \omega_{fg}$. In addition, \mathbf{k} and \mathbf{k}' are the photon wave vectors of the absorbed and emitted photons, respectively; $\mathbf{k} = \omega \boldsymbol{\eta}/c$ and $\mathbf{k}' = \omega' \boldsymbol{\eta}/c$. The first two terms represent the second-order contribution in perturbation theory (PT) of the coupling term $\mathbf{A} \cdot \mathbf{P}$, associated with the absorption of the photon ω and emission of ω' . In previous works reporting stimulated Compton and Raman scattering in atoms [32,33], it has been shown that the nondipole correction associated with $\mathbf{A} \cdot \mathbf{P}$ plays a negligible role. Therefore, the second-order term in PT associated with $\mathbf{A} \cdot \mathbf{P}$ can be treated in the dipole approximation. The third term in Eq. (15) refers to the nondipole contribution \mathbf{A}^2 . This term has been shown to play a crucial role in Compton and Raman scattering and is usually written

$$\langle f | e^{i(\mathbf{k} - \mathbf{k}') \cdot \mathbf{r}} | g \rangle = \langle f | e^{i\mathbf{Q} \cdot \mathbf{r}} | g \rangle, \quad (16)$$

where

$$\mathbf{Q} = \mathbf{k} - \mathbf{k}' = (\omega - \omega') \boldsymbol{\eta}/c \quad (17)$$

is the momentum transfer vector. As we will see below, $\omega - \omega'$ is of the order of a few a.u., so $(\omega - \omega')/c \ll 1$ and we can retain only the first two terms in the Taylor expansion of $e^{i\mathbf{Q} \cdot \mathbf{r}}$,

$$e^{i\mathbf{Q} \cdot \mathbf{r}} \simeq 1 + i\mathbf{Q} \cdot \mathbf{r}. \quad (18)$$

It is worth noting that both the ionization rate associated with \mathbf{A}^2 to first order in the momentum transfer and the rate associated with $\mathbf{A} \cdot \mathbf{P}$ to second order in PT vary quadratically with the field intensity.

From the above approximations, it is easy to extract the selection rules associated with $\mathbf{A} \cdot \mathbf{P}$ (in the dipole approximation) and \mathbf{A}^2 (up to $1/c$). We investigate all possible light-molecule configurations, with the polarization oriented along the z or x (or y) axis, i.e., parallel or perpendicular to the internuclear axis, respectively. For the transitions of second order in $\mathbf{A} \cdot \mathbf{P}$, the selection rules are (the polarization is indicated above the arrows, each arrow representing a one-photon transition)

$$\begin{aligned} X^1 \Sigma_g^+ &\xrightarrow{\mathbf{e}_z} \Sigma_u^+ \xrightarrow{\mathbf{e}_z} \Sigma_g^+, \\ X^1 \Sigma_g^+ &\xrightarrow{\mathbf{e}_x/\mathbf{e}_y} \Pi_u \xrightarrow{\mathbf{e}_x/\mathbf{e}_y} \Sigma_g^+, \Delta_g. \end{aligned} \quad (19)$$

Considering now the transition associated with \mathbf{A}^2 , we study the cases where the propagation direction $\boldsymbol{\eta}$ is along the z axis or along x or y . Treated in first order of perturbation theory and neglecting the corrections in $1/c^2$, the selection rules give

(the propagation direction is indicated above the arrow)

$$\begin{aligned} X^1\Sigma_g^+ &\xrightarrow{\eta_z} \Sigma_u^+, \\ X^1\Sigma_g^+ &\xrightarrow{\eta_x/\eta_y} \Pi_u. \end{aligned} \quad (20)$$

We note that the dipole transition leads to gerade (*g*) final states, while the nondipole one populates ungerade (*u*) states.

III. RESULTS AND DISCUSSION

We assume that the hydrogen molecule is initially in its ground state and that it interacts with an ultrashort x-ray pulse. The large energy bandwidth of the ultrashort pulse makes energetically accessible both stimulated Raman scattering (SRS) and stimulated Compton scattering, i.e., absorption and subsequent stimulated emission of photons, within a single pulse, leading to molecular excitation (SRS) and ionization close to threshold (SCS). For the present simulations, we use a linearly polarized Gaussian-shaped pulse with a full width at half maximum (FWHM) in time of 66 as (i.e., an energy bandwidth of $\simeq 2$ a.u.) and a peak intensity of 10^{18} W/cm². We note that the SCS process occurs because the energy bandwidth is much larger than the ionization threshold (0.6 a.u.). For a pulse duration of about 200 as, corresponding to an energy bandwidth (FWHM) equal to the ionization potential, SCS is still possible but the magnitude of the resulting peak would be smaller. For longer pulse durations, SCS would not be observed since two photons ω_1 and ω_2 with an energy difference of at least 0.6 a.u. cannot be found within the pulse bandwidth with sufficient intensity. All calculations are performed solving the TDSE, as explained in Sec. II A. We compute angle and energy differential ionization yields for pulses with three different central frequencies: $\omega_0 = 20, 40,$ and 60 a.u. (i.e., ≈ 544 eV, ≈ 1.1 keV, and ≈ 1.6 keV). As shown in the above-introduced studies of SCS in atoms, the dipole approximation is expected to break down at these photon energies and therefore we include both dipole and nondipole contributions through the Hamiltonian defined in Eq. (4). Due to the high photon energies, the Keldysh parameter γ [46], which marks the limit between the perturbative ($\gamma > 1$) and the nonperturbative ($\gamma < 1$) regime, is much larger than 1 and we therefore expect that the laser-molecule interaction process remains in the perturbative regime despite the high peak intensity values. In Fig. 1(a) we present a sketch of the SCS process in H₂, with the energy bandwidth of the pulse depicted as a purple shadow. In this single-pulse scheme, the photoabsorption and the stimulated emission processes lead to molecular ionization with an absorbed effective energy equal to the energy difference between two photons of energy within the bandwidth of the pulse: a more energetic photon that is absorbed and a slightly less energetic photon that is emitted. It should be noted that the same process can be induced by employing a scheme using longer pulse durations but combining two pulses with different colors [33]. Our scheme, employing a single attosecond pulse, is chosen to show the main features arising in molecular SCS using H₂ as a benchmark while keeping the computational effort within reasonable boundaries.

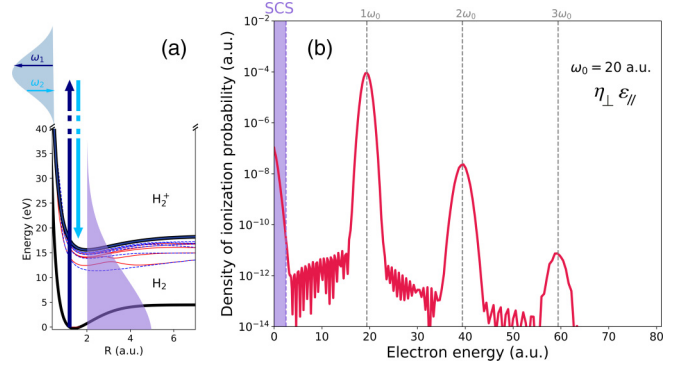


FIG. 1. (a) Schematic representation of the SCS process leading to the ejection of low-energy electrons. The thin blue dashed line and thin red solid line represent the lowest excited states of H₂ of $^1\Sigma_u^+$ and $^1\Sigma_g^+$ symmetries, respectively. The two thick lines represent the ground state of H₂ (lower line) and H₂⁺ (upper line). The energy bandwidth of the pulse is depicted by a blue shadow in the region of one-photon absorption (top left of the figure, not at scale) and by a purple shadow in the region of stimulated Raman and Compton scattering. Note that the shape of the energy bandwidths (magnitude of the energy bandwidth in the *x* direction provided on the abscissa in the figure) has been arbitrarily fixed for the sake of clarity. (b) Photoelectron spectrum for a 66-as pulse centered at $\omega_0 = 20$ a.u. (544 eV) for parallel polarization (ϵ_{\parallel}) and perpendicular propagation (η_{\perp}) of the light with respect to the molecular axis. The purple shadowed area indicates the energy region where SCS manifests (electron energies 0–2.5 a.u.). Vertical dashed lines indicate the position of the ATI absorption peaks, stemming from the absorption of one, two, and three photons.

A. Photoelectron spectra

The photoelectron spectrum resulting from the interaction of the hydrogen molecule with an x-ray pulse with the characteristics mentioned above and a central frequency $\omega_0 = 20$ a.u. (544 eV) is shown in Fig. 1(b). The light polarization vector is placed along the molecular axis and therefore the propagation direction is perpendicular to it, as illustrated in Fig. 2(a). The spectrum presents three large peaks associated with the absorption of one, two, and three photons from the H₂ ground state (indicated by vertical dashed lines in the figure), appearing at 19.4, 39.4, and 59.4 a.u. photoelectron energies. The ionization potential of H₂ at the equilibrium distance $R_e = 1.4$ a.u. is close to 0.6 a.u. These three strong peaks leading to single-photon ionization (ω_0) and above-threshold ionization (ATI) ($2\omega_0$ and $3\omega_0$) are perfectly reproduced

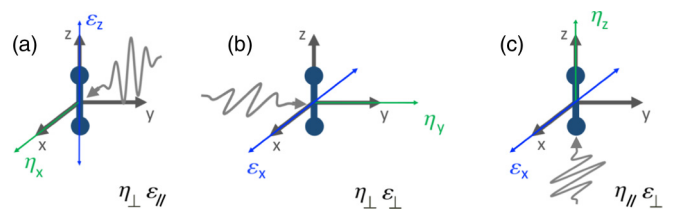


FIG. 2. The three configurations investigated in this article showing the light polarization (ϵ) and propagation (η) vectors with respect to the molecular axis (along the *z* axis): (a) configuration A, (b) configuration B, and (c) configuration C.

within the dipole approximation. Note that the oscillations observed in Fig. 1(b) appearing in between consecutive ATI peaks where the signal is very low are not physical but originate from the limited accuracy of the numerical approach. However, we also find a significant contribution close to the ionization threshold, at electron energies 0–2.5 a.u., which results from the absorption of a photon and the stimulated emission of another one and therefore corresponds to the SCS process. We have checked that the ionization rate in this region varies quadratically with the peak intensity, which confirms that, at these low photoelectron energies, the process is driven by two-photon transitions. We note that the choice of an intensity of 10^{18} W/cm² is made so that the SCS ionization signal is large enough to overcome the typical noise level of multicoincidence experiments. Asymmetries similar to those described in this work would be found at lower intensities, but due to the I^2 scaling, they would be much harder to detect due to the lower ionization probability. As explained above, the laser bandwidth ($\simeq 2$ a.u.) is larger than the ionization potential, energetically enabling electron emission over an energy range of the order of 1 a.u. above threshold. Although not shown here, similar photoelectron spectra are found for pulses centered at 40 and 60 a.u., i.e., every spectrum contains the one-photon and the ATI peaks as well as the increased yield due to SCS appearing close to threshold. However, while for the one-photon and ATI peaks the dipole contribution [see Eq. (4)] totally dominates, irrespective of the central energy of the pulse and of the molecular orientation, the SCS signal is modulated by both dipole and nondipole terms, whose relative contribution is strongly dependent on laser parameters and molecular orientation.

In Fig. 2 we show three typical light-molecule configurations for a diatomic homonuclear molecule. Obviously, for atomic systems, the spherical symmetry makes these three scenarios equivalent. It should be noted, however, that for the molecular case, assuming now the H₂ molecule along the z axis, there is a second equivalent configuration in each case by exchanging the x and y axes. For instance, in configuration A, the nondipole (A^2) rates are equal if the propagation proceeds along x or y , and only a rotation of $\pi/2$ of the azimuthal angle in the angular distributions would be expected for this term. For the same reasons, the dipole-induced signal is the same for B and C, and placing the polarization vector along the y axis for C again would only yield a $\pi/2$ rotation in the angular distributions. As a consequence, as we discuss next, one can achieve a different degree of control by manipulating the laser parameters for different molecular orientations.

We analyze the SCS signal, i.e., the electron energy region ranging from 0 to 2.5 a.u. [purple shadowed area in Fig. 1(b)] for the three possible configurations A, B, and C depicted in Fig. 2. The calculated photoelectron spectra for three pulses with different central frequencies ($\omega_0 = 20, 40, \text{ and } 60$ a.u.) are shown in Fig. 3. In addition to the total ionization yields, the figure shows the contributions from final states of different symmetries accessible by the two-photon SCS process.

We first focus on configuration A in Fig. 2: light polarization vector (ε_{\parallel}) parallel to the molecular axis, which is thus perpendicular to the light propagation direction (η_{\perp}), in this case along the x axis (η_x). In a two-photon process, the dipole operator will then couple the ground state of H₂, $X^1\Sigma_g^+$,

with electronic continuum states of $^1\Sigma_g^+$ symmetry, while the nondipole correction A^2 (calculated to first order in $1/c$) will populate states of $^1\Pi_u$ symmetry [see selection rules in Eqs. (19) and (20)].

The left column in Fig. 3 shows the ionization probability densities for the three pulses ($\omega_0 = 20, 40, \text{ and } 60$ a.u.) for configuration A ($\eta_{\perp}\varepsilon_{\parallel}$). We plot the contribution of dipole ($A \cdot P$ in green and purple solid lines for symmetries $^1\Sigma_g^+$ and $^1\Delta_g$, respectively) and nondipole (A^2 in red and orange dashed lines for $^1\Sigma_u^+$ and $^1\Pi_u$, respectively) coupling terms, as well as the total density of probability (thick blue solid line). For the three pulses, the nondipole contribution ($^1\Pi_u$) dominates over the dipole one ($^1\Sigma_g^+$) in the whole photoelectron energy range where SCS manifests, this trend being more pronounced as ω_0 increases. For the 20-a.u. pulse, the nondipole contribution is approximately one order of magnitude larger than the dipole counterpart for absorbed energies very close to threshold, but these contributions come closer as the photoelectron energy reaches 2.5 a.u. For 40 and 60 a.u. central frequencies, however, the nondipole contribution is two and three orders of magnitude larger, respectively, and it remains as the dominant term over the whole energy range up to 2.5 a.u. In fact, from Eq. (15) we can show that the dipole and nondipole probabilities scale as $1/\omega_0^8$ and $1/\omega_0^4$, respectively, for a given intensity. This propensity rule works very well for the three configurations shown in Fig. 3.

The unexpectedly low contribution of the dipole term in SCS has already been explained in previous studies [47] and can be understood as the result of the partial cancellation of the second-order dipole terms in Eq. (15) [33]. This partial cancellation of dipole amplitudes occurs for every molecular symmetry involved in the second-order dipole terms and therefore results in a decrease of this term for any orientation of the light with respect to the molecule. However, as shown below, the relative strengths of both dipole and nondipole contributions depend on the orientation of the molecular axis with respect to the polarization and propagation directions, so one finds a quite distinct behavior for each orientation.

For configuration B, illustrated in Fig. 2(b), the light polarization vector is now perpendicular to the molecular axis (ε_{\perp} along the x axis), while the propagation direction is still perpendicular to it (η_{\perp} along the y axis). The coupling terms associated with nondipole corrections (A^2) are thus the same as in the previous configuration, leading to a population of final states of $^1\Pi_u$ symmetry. Therefore, the ionization probability densities associated with $^1\Pi_u$ final states in Figs. 3(b), 3(e), and 3(h) are the same as those resulting from configuration A in Figs. 3(a), 3(d), and 3(g). However, the dipole selection rules for a two-photon process now allow for transitions to $^1\Sigma_g^+$ and $^1\Delta_g$ final-state symmetries, undergoing a second-order process through intermediate $^1\Pi_u$ states [see Eq. (19)]. As has been shown in previous works on H₂ [39,48], dipole couplings connecting the ground and the excited states of H₂ are significantly larger when the molecule is perpendicular to the polarization vector. Consequently, the dipole contribution in configuration B is larger than that in the parallel case (configuration A). As a result, for a 20-a.u. pulse in configuration B ($\eta_{\perp}\varepsilon_{\perp}$) [Fig. 3(b)], the SCS signal is now dominated by the dipole terms over the whole range of photoelectron energies. However, according to the scaling

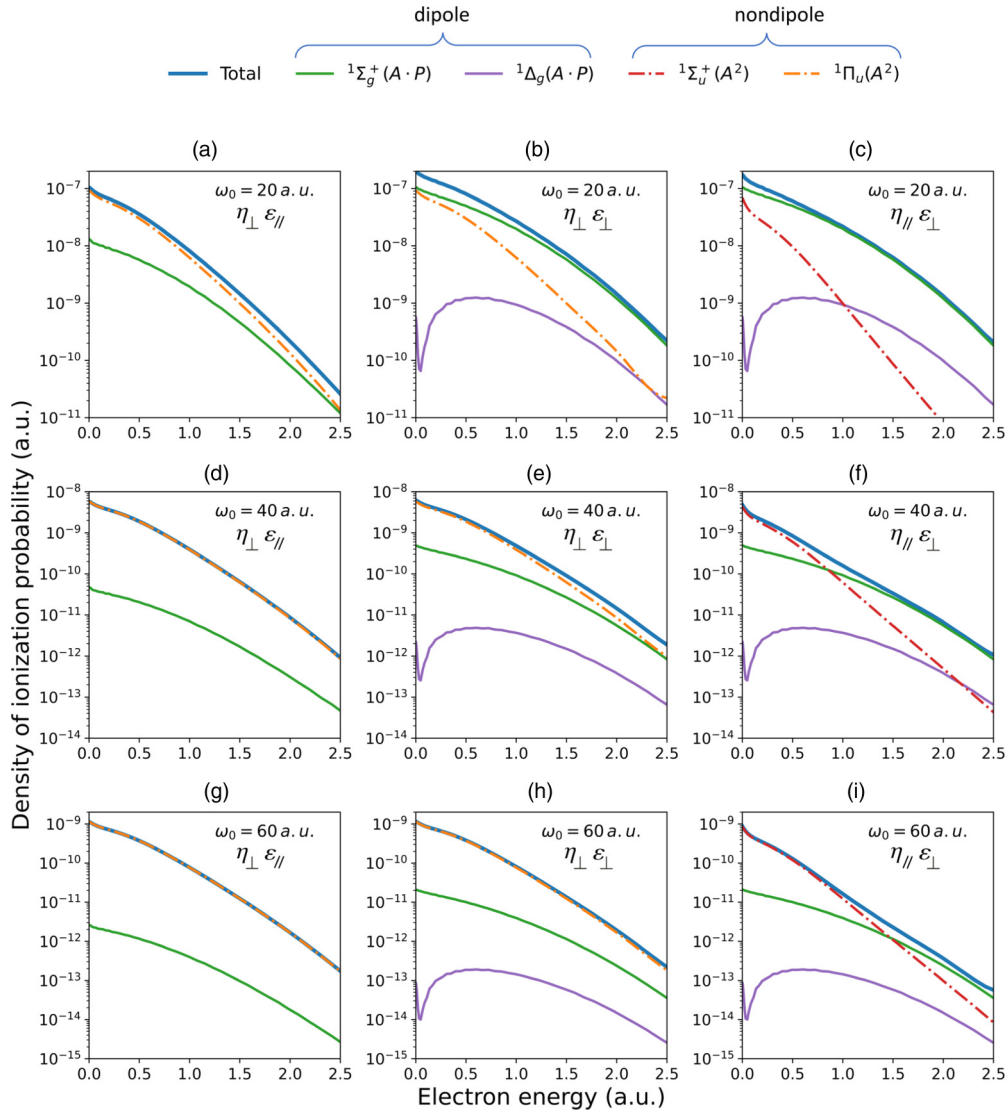


FIG. 3. Photoelectron spectra for three different pulses, centered at (a)–(c) $\omega_0 = 20$ a.u., (d)–(f) $\omega_0 = 40$ a.u., and (g)–(i) $\omega_0 = 60$ a.u. Each column corresponds to a given configuration for the light polarization and propagation directions with respect to the molecular axis as plotted in Fig. 2. Thick blue lines are the total ionization yields. Green and purple solid lines are the contributions from the dipole terms. Red and orange dash-dotted lines are the contributions from the nondipole terms.

laws mentioned above, the dipole contributions scale as $1/\omega_0^8$ while the nondipole ones scale as $1/\omega_0^4$, so dipole-induced transitions become less important for the larger central frequencies. We thus find that, for 40- and 60-a.u. pulses [Figs. 3(e) and 3(h)], the nondipole corrections are still the dominant contributions to the SCS signal.

For configuration C, depicted in Fig. 2(c), the light polarization vector is kept perpendicular to the molecular axis (ϵ_\perp along the x axis as in configuration B), but with the propagation direction parallel to it (η_\parallel). As for the dipole terms, the nondipole correction terms (A^2) become smaller when the direction of the corresponding operator is parallel to the molecular axis. Consequently, while the dipole contribution remains as in configuration B, the nondipole correction will decrease significantly with respect to the previous case. In configuration C, for the 20-a.u. pulse [Fig. 3(c)], the dipole contribution is the dominant channel in the whole energy

range. For the 40-a.u. pulse [Fig. 3(f)], the nondipole corrections are still dominant up to photoelectron energies of 1.0 a.u. and they are overcome by the dipole contributions as the electron energy becomes larger. Even for the 60-a.u. pulse, where the nondipole terms are more than an order of magnitude larger close to threshold, the dipole contribution becomes quickly dominant, overtaking the nondipole contribution for photoelectron energies above 1.5 a.u.

Concisely, Fig. 3 represents a quick summary of the interplay between the underlying mechanisms responsible for SCS and their relative importance as a function of energy and molecular orientation. In brief, the larger the central frequency of the pulse and the smaller the photoelectron energy, the more probable the observation of nondipole-induced SCS. More interestingly, the nondipole SCS becomes dominant over the dipole-induced counterpart when the molecular axis is perpendicular to the light propagation direction, being even more

favorable when the light polarization direction is kept parallel to the molecular axis.

Note that for every light-molecule configuration and every pulse investigated here, the dipole terms become quickly dominant for electron energies larger than 2.5 a.u. so that the largest ionization probability corresponds to the one-photon absorption process (first-order dipole) at $E_e = \omega_0 - \mathcal{I}$ (with \mathcal{I} the ionization energy being ≈ 0.6 a.u.), leading to the peak at $1\omega_0$ in Fig. 1(b). As expected, the SCS probability is of the order of the second-order dipole transition at around $E_e = 2\omega_0 - \mathcal{I}$ [first ATI peak, at $2\omega_0$, as shown in Fig. 1(b)], a feature also observed in atoms. However, the two-center character of the molecule provides a different aspect in SCS and ATI: the fact that the total angular momentum is not conserved and consequently the ejected electron is described by a coherent superposition of spherical harmonics with the same m but different l . Therefore, in the molecular case, the relative contribution of the second-order dipole terms does not follow the patterns found in atoms, which in the case of an initial state with $l = 0$ predicts population of $l = 0$ (S) and $l = 2$ (D) states. The calculations show that stimulated Raman and Compton processes in the hydrogen atom favor the $l = 0$ channel over the $l = 2$ one [32,35]. Instead, for example, in the case of perpendicular polarization, we have found a larger probability for $^1\Sigma_g^+$ with $l = 4$.

B. Molecular frame photoelectron angular distributions

From the experimental point of view, it is not possible to retrieve from the photoelectron spectra the different contributions of dipole- and nondipole-induced SCS probabilities or the relative weight associated with each final symmetry or partial waves. However, the interplay between these paths can be experimentally captured when measuring the angular distributions of the emitted electrons. These are very sensitive to small variations in the relative contributions from distinct quantum paths. The dominant final symmetry will lead to an electron emission favoring some specific directions, and detailed information on the dominant terms can be experimentally retrieved to a large extent from the molecular frame photoelectron angular distributions (MFPADs).

The MFPADs shown in Fig. 4 have been obtained solving the TDSE with the full Hamiltonian [see Eq. (4)], after integrating over electron energies in the range 0–2.5 a.u. [purple shadowed region in Fig. 1(b) or, equivalently, the whole energy range shown in every panel in Fig. 3]. For the sake of clarity, we follow the same layout as in Fig. 3. Each column corresponds to a given light configuration with respect to the molecular axis, configurations A ($\eta_{\perp}\epsilon_{\parallel}$), B ($\eta_{\perp}\epsilon_{\perp}$), and C ($\eta_{\parallel}\epsilon_{\perp}$) as depicted in Fig. 2. Each row corresponds to the results for a given pulse, centered at $\omega_0 = 20, 40,$ and 60 a.u. One can see that every MFPAD, for the three limiting cases, presents a symmetry plane for the electron emission defined by the light, i.e., the plane containing the polarization and propagation vectors.

When nondipole-induced SCS dominates, e.g., at 60 a.u. in configuration A (bottom left panel in Fig. 4), the electrons are emitted following a cosine-squared-like distribution with respect to the light propagation direction (η_x) and with a cylindrical symmetry around this axis, compatible with a final $^1\Pi_u$

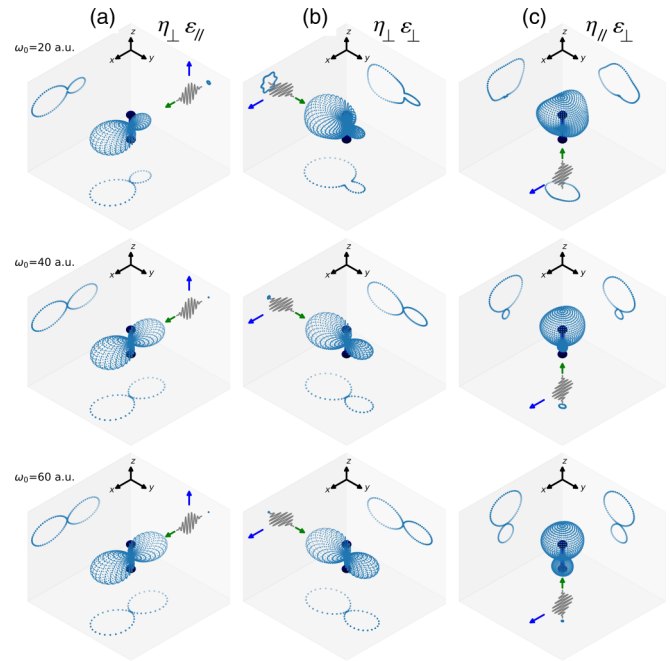


FIG. 4. Molecular frame photoelectron angular distribution integrated over electron energies over the range 0–2.5 a.u. [purple shadowed region in Fig. 1(b), or equivalently the whole energy range shown in every panel in Fig. 3]. Each row corresponds to the results for a given pulse, centered at $\omega_0 = 20, 40,$ and 60 a.u. Each column corresponds to a given light configuration with respect to the molecular axis, configurations $A, B,$ and C as depicted in Fig. 2.

symmetry of the system. The H_2^+ ion is left in its ground state $1s\sigma_g$ and electrons are emitted with odd angular momenta, $l = 1$ being the dominant partial wave. As the photon energy

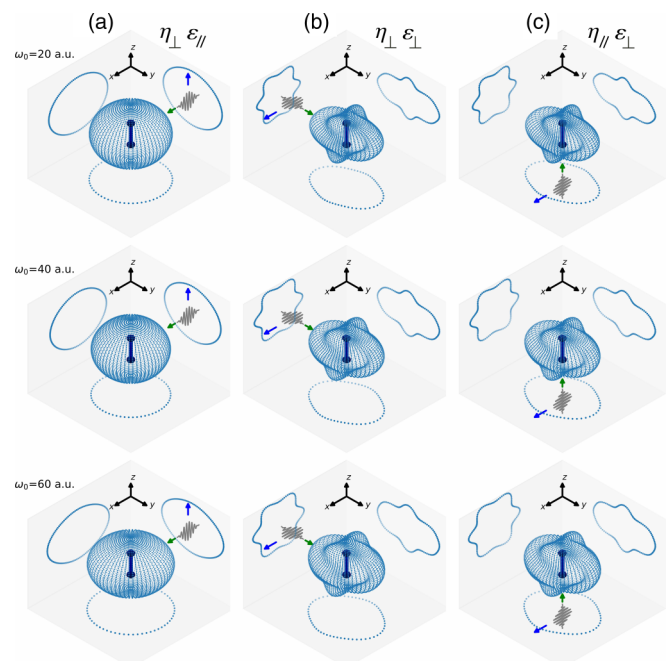


FIG. 5. Same as Fig. 4, but retrieving the MFPADs within the dipole approximation.

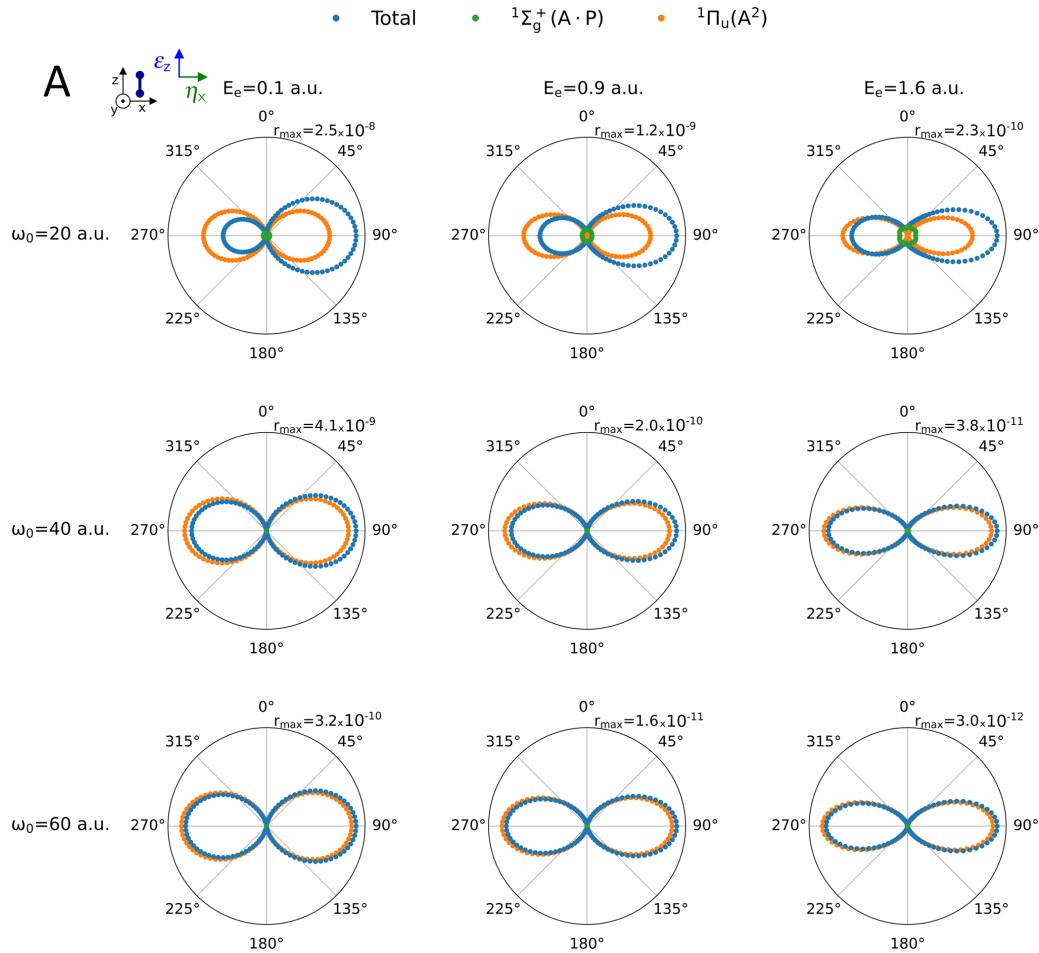


FIG. 6. Two-dimensional MFPADs for configuration A ($\eta_{\perp}\varepsilon_{\parallel}$) with the polarization vector along the z axis and the propagation along x (see the inset in the top left of the figure). The two-dimensional projection is performed in the plane defined by the light vectors and positioned at the molecular center of mass. Together with the MFPADs, the incoherent contributions associated with the different open channels, i.e., all accessible symmetries through dipole ($^1\Sigma_g^+$) and nondipole transitions ($^1\Pi_u$), are given and indicated in the legend.

decreases, the dipole contribution increases (see Fig. 3) and the interference between the different quantum paths distorts the distribution, which becomes asymmetric along the propagation direction, i.e., with respect to the plane containing the polarization vector and perpendicular to the propagation direction.

This symmetry breaking in the photoelectron emission results from the coherent contribution of dipole-induced transitions populating $^1\Sigma_g^+$ states and nondipole-induced transitions reaching the $^1\Pi_u$ symmetry. This effect becomes more apparent for the lower photon energies as shown in the left column in Fig. 4. The same trend is found in the middle column of Fig. 4, for configuration B ($\eta_{\perp}\varepsilon_{\perp}$). Again, since the SCS signal is dominated by the nondipole term (A^2), the electron emission for the highest photon energies mostly follows the propagation direction η_y , with a cylindrical symmetry around it. A more pronounced asymmetry is now found in the electron emission for $\omega_0 = 20$ a.u., because (see Fig. 3) dipole and nondipole terms coherently contribute significantly to the electron emission at different angles, while at 60 a.u. it is mostly the nondipole terms that are predominant. Note that the angular distributions for 60 a.u. in configurations A and B are rather similar, following the propagation direction

η . This is explained by the fact that the nondipole contribution in the $^1\Pi_u$ states is the dominant one and it is indistinguishable in the photoelectron spectra as shown in Fig. 3. It can be only distinguished because the propagation direction is placed along the x axis for configuration A, while for configuration B it follows the y axis. Interestingly, for configuration B, the asymmetric electron emission is favored in the backward direction with respect to the propagation direction. Finally, in configuration C, the asymmetric photoelectron emission with respect to the plane containing the polarization vector and perpendicular to the propagation is found for every pulse because both dipole and nondipole terms significantly contribute to the ionization yields in the SCS region for all central frequencies ω_0 .

Electron emission angular asymmetries have been explored over the years in atoms and molecules as the result of the coherent superposition of states with different gerade or ungerade symmetries or, equivalently, with scattered electrons carrying even or odd angular momenta. This can already be achieved within a regime where the dipole approximation remains valid by combining light sources with two different colors that induce interferences between processes occurring at different orders, for instance, using an ultrashort UV or

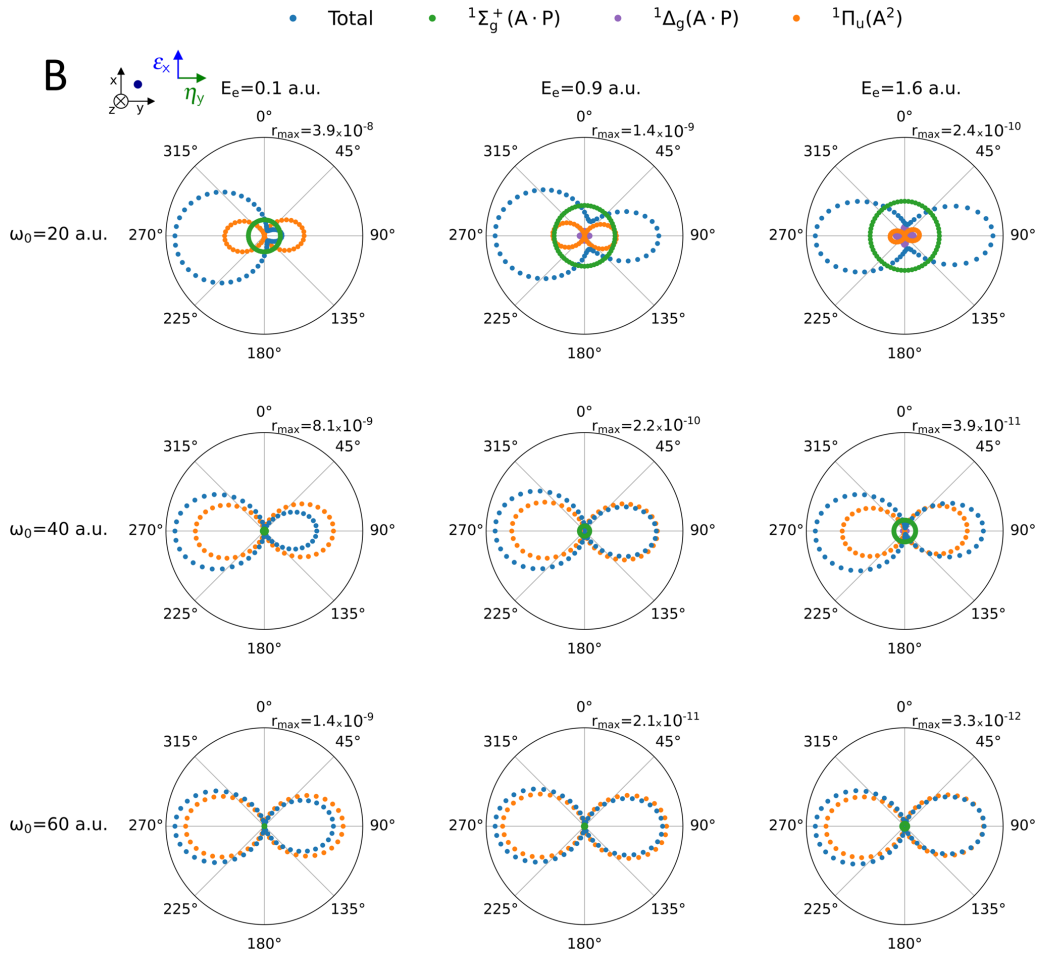


FIG. 7. Same as Fig. 6 for configuration *B*, with extra channel ${}^1\Delta_g$ plotted in purple.

XUV pulse and an IR field [49] or employing a free-electron laser at two different XUV or soft-x-ray frequencies such that the one-photon absorption of ω_1 can reach the same energies as the two-photon absorption of $\omega_2 = \omega_1/2$, but emitting electrons with different angular momenta [50]. In the present SCS process, the different final symmetries are reached at the same (second) order because two different operators ($\mathbf{A} \cdot \mathbf{P}$ and \mathbf{A}^2) acting over the ground state of the target are at play on equal footing. Moreover, as we will explain in the following, the molecular orientation provides an extra parameter of control with respect to atoms.

In order to better illustrate the properties of nondipole-induced molecular SCS, we also show the MFPADs that are obtained in a simulation performed within the dipole approximation. Figure 5 shows these MFPADs for the three pulses and the three configurations, keeping the layout of Figs. 3 and 4. We can see at a glance that the dipole approximation predicts quite distinct distributions. First, for a given configuration, Fig. 5 shows that the shape of the distributions barely varies with the central frequency ω_0 in the dipole approximation. Also, configurations *B* and *C* are now equivalent, as already explained. Since the only coupling terms are those involving the dipole operator ($\mathbf{A} \cdot \mathbf{P}$) following $\boldsymbol{\varepsilon}_x$ [Figs. 2(b) and 2(c)], the angle-resolved SCS signal is thus exactly the same for configurations *B* and *C*. The complex but still symmetric pattern for these angular distributions is due in general

to the multicenter character of the molecule. For configuration *A*, the dipole-induced MFPADs in the SCS region are quite atomiclike (which favors electron emission with $l = 0$, as already mentioned). For this configuration, the second-order process ${}^1\Sigma_g^+ \rightarrow {}^1\Sigma_u^+ \rightarrow {}^1\Sigma_g^+$ [see Eqs. (19)] favors the contribution of final electron emission with $l = 0$ associated with ${}^1\Sigma_g^+(1s\sigma_g, l = 0)$. This is consistent with the spherical distribution in the electron emission found in configuration *A* for every pulse (left column in Fig. 5). For configurations *B* and *C* in the dipole approximation, the predominant channel ${}^1\Sigma_g^+$ is populated through the second-order process ${}^1\Sigma_g^+ \rightarrow {}^1\Pi_u \rightarrow {}^1\Sigma_g^+$. We have found that the largest contribution comes from electrons with $l = 0$, but $l = 2$ has a non-negligible contribution. These two channels contribute, resulting in the main features shown in the symmetric MFPADs shown in the middle and right columns in Fig. 5. It should be noted that the ${}^1\Delta_g$ states are also populated (see Fig. 3), and even though the probability is a couple of orders of magnitude smaller, the resulting MFPADs shown for configurations *B* and *C* are also partly shaped by the ${}^1\Delta_g$ contribution. Furthermore, if we compare in Figs. 4 and 5 the cuts in the two planes containing the propagation direction, one perpendicular to the polarization vector and the other parallel, we clearly see that the nearly cylindrical symmetry around the propagation direction $\boldsymbol{\eta}$ is absent in the dipole approximation. The quite distinct photoelectron distributions

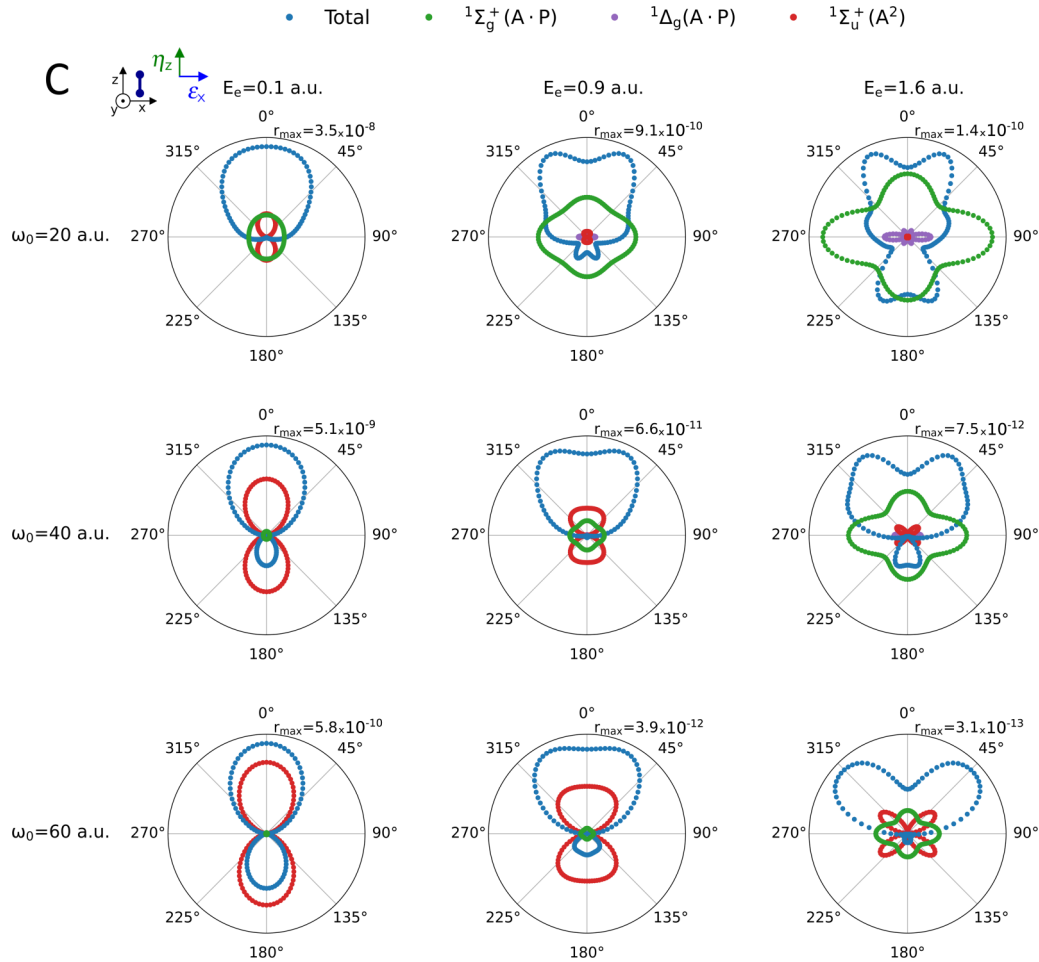


FIG. 8. Same as Fig. 6 for configuration C.

of Figs. 4 and 5 thus imply that experimentally it would be possible to disentangle the dipole- and nondipole-induced SCS contributions, but also between the relative contributions of specific symmetries. For a more detailed analysis of the resulting angular dependences, we also extract the MFPADs for specific photoelectron energies, including all dipole and nondipole terms. Instead of integrating over the whole electron energy range, we now inspect the angular distributions for three specific photoelectron energies $E_e = 0.1, 0.9$, and 1.6 a.u. and for completeness in our analysis, we show them for the three pulses ($\omega_0 = 20, 40$, and 60 a.u.) and the three configurations presented in Fig. 2. Figure 6 shows the angular distributions for the three pulses and the three photoelectron energies for the light-molecule configuration A ($\eta_{\perp}\varepsilon_{\parallel}$). The same results are shown in Fig. 7 for configuration B ($\eta_{\perp}\varepsilon_{\perp}$) and in Fig. 8 for C ($\eta_{\parallel}\varepsilon_{\perp}$). We now include not only the resulting angular distribution but also the incoherent contribution of each accessible final symmetry. To better visualize each contribution, instead of a three-dimensional plot, we now plot only a cut of the angular distribution containing the symmetry plane given by the light, i.e., the plane defined by the polarization and the propagation vector: for configuration A in Fig. 6 a cut in the xz plane, for configuration B in Fig. 7 a cut in the xy plane, and for configuration C in Fig. 8 a cut in the xz plane.

As we have seen in the left column of Fig. 3, for configuration A, nondipole-induced SCS dominates at any photoelectron energy for the three pulses, with a larger predominance for large ω_0 and for low electron energy. As a result, we can see in Fig. 6 an almost symmetric electron emission for central frequencies of 40 and 60 a.u. We see the reflection symmetry relative to the zy plane associated with the A^2 term since, to first order in $1/c$, this term reduces to $A(t)F(t)\sum_{i=1,2}x_i/c$ [see Eq. (4)], leading to a forward-backward asymmetry of the electron emission along the x axis. This symmetry is broken in the total MFPAD (blue dots). As expected, as the dipole term becomes larger for a photon energy of 20 a.u., the electron asymmetry clearly manifests, being more pronounced for the lowest electron energy (0.1 a.u.). An interesting feature shown in Fig. 6 is the trend found as the electron energy increases, where the MFPAD becomes more directional towards the propagation vector η_x .

In Fig. 7 we show the corresponding MFPADs for configuration B. Now, for every photon and electron energy, the asymmetric electron emission is appreciable, being larger at a 20 a.u. photon energy and lower electron energies, where dipole and nondipole terms are comparable in magnitude. We also clearly see that the electron emission is in the backward direction with respect to the propagation direction, a feature already noted in the discussion of Fig. 4, which is more

pronounced when the nondipole contribution is of the order of magnitude of the dipole one.

For configuration *C*, in Fig. 8, one finds the strongest variation in the MFPADs with pulse and electron energies, as was expected from the remarkable competition between channels shown in Fig. 3. We focus on the 20-a.u. pulse, i.e., the top row in Fig. 8. For the electron energy of 0.1 a.u. closest to threshold, the largest asymmetry is found as a result of the coherent superposition of the $^1\Sigma_g^+$ (green dots) and $^1\Sigma_u^+$ (red dots) states populated through the dipole $\mathbf{A} \cdot \mathbf{P}$ and nondipole \mathbf{A}^2 terms, respectively. In this case, a pure dipole transition would lead to almost spherical emission associated with $^1\Sigma_g^+$, where the H_2^+ is left behind in its $X^2\Sigma_g^+(1s\sigma_g)$ ground state and the electron is emitted as a combination of even angular momenta, mostly $l = 0$ as revealed in the distribution in green dots. The $^1\Sigma_u^+$ symmetry (red dots) reached through the nondipole terms leads to an electron emission mostly given by an $l = 1$ angular momentum. Because these two amplitudes now present similar magnitudes, one finds a highly asymmetric electron emission. For larger electron energies, 0.9 and 1.6 a.u., we observe that a pure dipole transition into the $^1\Sigma_g^+$ state (green dots) already produces the complex but still symmetric pattern previously mentioned, because a higher angular momentum ($l = 2$) is also contributing. Moreover, we see an increased probability associated with the dipole transition into the $^1\Delta_g$ states (purple dots). Even though the dipole-driven amplitudes are significantly smaller than the nondipole-induced ones, the coherent sum leads to a noticeable asymmetry as seen in the bottom left panel of Fig. 8. We now focus on the left column of Fig. 8 to examine the variation of the MFPADs for a given electron energy as we increase the central photon energies ω_0 . As the photon energy increases, the nondipole term (\mathbf{A}^2 in red dots) also increases, reaching values orders of magnitude larger than the dipole counterpart, leading to a less pronounced asymmetry. As illustrated in Fig. 8, the largest asymmetries are found when the relative amplitudes reach similar values in specific electron emission directions, i.e., for the 20-a.u. pulse with the lowest electron energies (e.g., 0.1 a.u., top left panel in Fig. 8) or for the 60-a.u. pulse for the largest electron energies (e.g., 1.6 a.u., bottom right panel in Fig. 8).

IV. CONCLUSION

We have investigated theoretically close-to-threshold ionization of H_2 by stimulated Compton scattering using an ultrashort soft-x-ray pulse. As a proof of concept, we provided

simulations within a nonperturbative nonrelativistic approximation with frozen nuclei at the equilibrium distance. Stimulated Compton scattering can be induced by using soft-x-ray pulses such as those currently generated in free-electron laser facilities. The present schemes could be achieved with a single pulse having a duration of several tens of attoseconds or, alternatively, with two collinear soft-x-ray pulses of different colors. We have simulated the angle- and energy-resolved photoionization yields that would result after the interaction of H_2 with three different pulses of 66-as duration and 10^{18} W/cm², centered around photon energies of 20, 40, and 60 a.u., respectively. We have checked that, under these conditions, the perturbative regime holds and therefore the SCS rates vary quadratically with the intensity. The large energy bandwidth of the pulse allows for the absorption and subsequent emission of photons leading to ionization close to threshold. We have shown that with these laser parameters molecular SCS proceeds through both dipole- and nondipole-induced transitions. As a consequence, the coherent emission of electrons through different quantum paths leads to controllable asymmetric electron emission. We have shown that molecular SCS provides three knobs of control, i.e., (i) the molecular axis, (ii) the light polarization, and (iii) the light propagation direction, thus offering a much richer scenario than the atomic SCS. We hope that the present study will stimulate experimental investigations of molecular SCS by combining subfemtosecond XFEL pulses with multicoincidence detection techniques.

ACKNOWLEDGMENTS

This work was supported by the European COST Action AttoChem No. CA18222, the French National Research Agency in the frame of the Investments for the Future Programme IdEx Bordeaux, LAPHIA (Program No. ANR-10-IDEX-03-02), and the Spanish Ministry of Science and Innovation MICINN through Project No. PDI2019-105458RB-I00, the Severo Ochoa Programme for Centres of Excellence in R&D (Program No. SEV-2016-0686) and the María de Maeztu Programme for Units of Excellence in R&D (Program No. CEX2018-000805-M). The authors thank the University of Bordeaux for providing access to the Mésocentre de Calcul Intensif Aquitain and the MareNostrum in the Barcelona Supercomputing Center through the Spanish Supercomputing Network and in the Centro Computación Científica at UAM.

-
- [1] W. Ackermann *et al.*, *Nat. Photon.* **1**, 336 (2007).
 - [2] P. Emma *et al.*, *Nat. Photon.* **4**, 641 (2010).
 - [3] S. Jamison, *Nat. Photon.* **4**, 589 (2010).
 - [4] T. Ishikawa *et al.*, *Nat. Photon.* **6**, 540 (2012).
 - [5] M. Allaria *et al.*, *Nat. Photon.* **6**, 699 (2012).
 - [6] H.-S. Kang *et al.*, *Nat. Photon.* **11**, 708 (2017).
 - [7] T. Tschentscher, C. Bressler, J. Grünert, A. Madsen, A. P. Mancuso, M. Meyer, A. Scherz, H. Sinn, and U. Zastra, *Appl. Sci.* **7**, 592 (2017).
 - [8] C. J. Milne *et al.*, *Appl. Sci.* **7**, 720 (2017).
 - [9] C. Bostedt, S. Boutet, D. M. Fritz, Z. Huang, H. J. Lee, H. T. Lemke, A. Robert, W. F. Schlotter, J. J. Turner, and G. J. Williams, *Rev. Mod. Phys.* **88**, 015007 (2016).
 - [10] E. A. Seddon *et al.*, *Rep. Prog. Phys.* **80**, 115901 (2017).
 - [11] L. Young *et al.*, *J. Phys. B* **51**, 032003 (2018).
 - [12] E. Hemsing, G. Stupakov, D. Xiang, and A. Zholents, *Rev. Mod. Phys.* **86**, 897 (2014).
 - [13] S. Huang, Y. Ding, Y. Feng, E. Hemsing, Z. Huang, J. Krzywinski, A. A. Lutman, A. Marinelli, T. J. Maxwell, and D. Zhu, *Phys. Rev. Lett.* **119**, 154801 (2017).

- [14] M. Hentschel, R. Kienberger, C. Spielmann, G. A. Reider, N. Milosevic, T. Brabec, P. Corkum, U. Heinzmann, M. Drescher, and F. Krausz, *Nature (London)* **414**, 509 (2001).
- [15] T. Gaumnitz, A. Jain, Y. Pertot, M. Huppert, I. Jordan, F. Ardana-Lamas, and H. J. Wörner, *Opt. Express* **25**, 27506 (2017).
- [16] R. Bartels, S. Backus, I. Christov, H. Kapteyn, and M. Murnane, *Chem. Phys.* **267**, 277 (2001).
- [17] M.-C. Chen *et al.*, *Proc. Natl. Acad. Sci. USA* **111**, E2361 (2014).
- [18] N. Hartmann *et al.*, *Nat. Photon.* **12**, 215 (2018).
- [19] J. Duris *et al.*, *Nat. Photon.* **14**, 30 (2020).
- [20] H. Fukuzawa *et al.*, *Nat. Commun.* **10**, 2186 (2019).
- [21] S. Li, T. Driver, O. Alexander, B. Cooper, D. Garratt, A. Marinelli, J. P. Cryan, and J. P. Marangos, *Faraday Discuss.* **228**, 488 (2021).
- [22] A. A. Lutman, R. Coffee, Y. Ding, Z. Huang, J. Krzywinski, T. Maxwell, M. Messerschmidt, and H.-D. Nuhn, *Phys. Rev. Lett.* **110**, 134801 (2013).
- [23] G. De Ninno, B. Mahieu, E. Allaria, L. Giannessi, and S. Spampinati, *Phys. Rev. Lett.* **110**, 064801 (2013).
- [24] T. Hara *et al.*, *Nat. Commun.* **4**, 2919 (2013).
- [25] S. Serkez *et al.*, *Appl. Phys.* **10**, 2728 (2020).
- [26] G. Doumy, C. Roedig, S. K. Son, C. I. Blaga, A. D. DiChiara, R. Santra, N. Berrah, C. Bostedt, J. D. Bozek, P. H. Bucksbaum, J. P. Cryan, L. Fang, S. Ghimire, J. M. Glowina, M. Hoener, E. P. Kanter, B. Krassig, M. Kuebel, M. Messerschmidt, G. G. Paulus *et al.*, *Phys. Rev. Lett.* **106**, 083002 (2011).
- [27] M. Fuchs, *Nat. Phys.* **11**, 964 (2015).
- [28] H. Dörner, V. Mergel, O. Jagutzki, L. Spielberger, J. Ullrich, R. Moshhammer, and H. Schmidt-Böcking, *Phys. Rep.* **330**, 95 (2000).
- [29] M. Kircher *et al.*, *Nat. Phys.* **16**, 756 (2020).
- [30] S. Grundmann *et al.*, *Science* **370**, 339 (2020).
- [31] H. Bachau and M. Dondera, *Europhys. Lett.* **114**, 23001 (2016).
- [32] M. Dondera, V. Florescu, and H. Bachau, *Phys. Rev. A* **95**, 023417 (2017).
- [33] H. Bachau, M. Dondera, and V. Florescu, *Phys. Rev. Lett.* **112**, 073001 (2014).
- [34] M. Dondera, V. Florescu, and H. Bachau, *Phys. Rev. A* **90**, 033423 (2014).
- [35] M. Dondera and H. Bachau, *Phys. Rev. A* **85**, 013423 (2012).
- [36] A. Sopena, A. Palacios, F. Catoire, H. Bachau, and F. Martín, *Commun. Phys.* **4**, 253 (2021).
- [37] H. Bachau, E. Cormier, P. Decleva, J. E. Hansen, and F. Martín, *Rep. Prog. Phys.* **64**, 1815 (2001).
- [38] F. Martín, *J. Phys. B* **32**, R197 (1999).
- [39] A. Palacios, J. L. Sanz-Vicario, and F. Martín, *J. Phys. B* **48**, 242001 (2015).
- [40] A. Palacios, S. Barmaki, H. Bachau, and F. Martín, *Phys. Rev. A* **71**, 063405 (2005).
- [41] R. Anzaki, Y. Shinohara, T. Sato, and K. L. Ishikawa, *Phys. Rev. A* **98**, 063410 (2018).
- [42] A. D. Bandrauk, F. Fillion-Gourdeau, and E. Lorin, *J. Phys. B* **46**, 153001 (2013).
- [43] H. A. Kramers and W. Heisenberg, *Z. Phys.* **31**, 681 (1925).
- [44] I. Waller, *Z. Phys.* **51**, 213 (1928).
- [45] M. Gavrilu, *Phys. Rev. A* **6**, 1348 (1972).
- [46] L. V. Keldysh, *Sov. Phys. JETP* **20**, 1307 (1965).
- [47] P. Eisenberger and P. M. Platzman, *Phys. Rev. A* **2**, 415 (1970).
- [48] O. A. Fojón, J. Fernández, A. Palacios, R. D. Rivarola, and F. Martín, *J. Phys. B* **37**, 3035 (2004).
- [49] R. Y. Bello, F. Martín, and A. Palacios, *Faraday Discuss.* **228**, 378 (2021).
- [50] K. C. Prince *et al.*, *Nat. Photon.* **10**, 176 (2016).